Supporting Information

Zero-Standby Power Hydrogen Sensing Using Event-Driven Micromechanical Switches

S M Jahadun Nobi, Eric Herrmann, Zhixiang Huang, Sai Rahul Sitaram, Kyle Laskowski, and Xi Wang*

Palladium Hydrogen interaction:

Palladium (Pd) exhibits a unique metal–hydrogen interaction and has the exceptional ability to dissolve large quantities of H_2, identified by Graham in 1866.[1] The H_2 absorption process in Pd occurs via gas-phase or wet-chemical reactions and follows a two-step process: surface adsorption followed by diffusion into the face-centered cubic (fcc) lattice. Initially, hydrogen atoms adsorb onto the Pd surface, forming under-potentially deposited hydrogen (HUPD). Absorption then proceeds via an indirect mechanism, where HUPD acts as a precursor, transitioning through subsurface hydrogen before integrating into the bulk Pd hydride.[2, 3] Once the Pd surface is saturated with adsorbed hydrogen (H_{ads}), H_2 evolution reaction begins, following either the Heyrovsky or Tafel mechanism:

$$H^+ + Pd + e^- \rightleftharpoons PdH_{UPD} \rightleftharpoons PdH_{ads} \qquad (S1)$$

$$PdH_{ads} + H^+ + e^- \rightleftharpoons H_2\ (Hervosky) \qquad (S2)$$

$$2PdH_{ads} \rightleftharpoons 2Pd + H_2\ (Tafel) \qquad (S3)$$

The Pd-H system exhibits two distinct phases at ambient conditions. At low hydrogen gas pressure, Pd forms a solid-solution α phase (PdH_x, $x < 0.03$ at room temperature). As the pressure increases, a first-order phase transition occurs at a plateau pressure, leading to significant hydrogen absorption and lattice expansion, resulting in the hydride β phase (PdH_x, $x > 0.03$ at room temperature). The Pd-H lattice maintains its fcc structure, with hydrogen atoms occupying octahedral interstitial sites. Under high-temperature or high-pressure conditions, partial occupation

of tetrahedral sites may also occur.[2, 3] This expansion is isotropic due to the symmetrical arrangement of available bonding sites for H_2 in the fcc structure of Pd. As Pd demonstrates high compatibility with MEMS, therefore, Pd is the material of choice for switch structures in this study.[4, 5]

Design and Simulation:

Palladium (Pd) is utilized as the sensing material in the hydrogen sensing mechanism based on a micromechanical bistable switch. We employed a four-layer cantilever structure (chromium, copper, chromium, and palladium) as this multilayer configuration offers tunable control over the cantilever's curvature. The final curvature of the cantilever is governed by the combined residual stresses arising from the fabrication in all four layers. To estimate the curvature after the release process, we applied the model proposed by Nikishkov (see Equation S4), which accounts for the residual stress contributions of multilayered structures. The curvature (κ) of the cantilever is calculated as:

$$\kappa = \frac{3\sum_{i=1}^{4}\frac{E_i t_i}{(1-\nu_i^2)}(y_i + y_{i-1} - 2y_b)\{c - (1+\nu_i)\epsilon_i^0\}}{2\sum_{i=1}^{4}\frac{E_i t_i}{(1-\nu_i^2)}[y_i^2 + y_i y_{i-1} + y_{i-1}^2 - 3y_b(y_i + y_{i-1} - y_b)]} \qquad (S4)$$

Here, $y_b = \frac{\sum_{i=1}^{4}\frac{E_i t_i}{(1-\nu_i^2)}(y_i + y_{i-1})}{2\sum_{i=1}^{4}\frac{E_i t_i}{(1-\nu_i^2)}}$, $c = \frac{\sum_{i=1}^{4}\frac{E_i t_i (1+\nu_i)\epsilon_i^0}{(1-\nu_i^2)}}{\sum_{i=1}^{4}\frac{E_i t_i}{(1-\nu_i^2)}}$, $\epsilon^0 = \epsilon_{Pd}$ for the Pd layer. The material properties involved are Young's modulus E_i, Poisson's ratio ν_i, film thickness t_i, and initial strain ε_i of the i th layer.

In a hydrogen-rich environment, Pd absorbs hydrogen and undergoes a phase transition, leading to volumetric expansion. This alters the internal stress in the Pd layer and leads to a change in the curvature of the cantilever. The correlation between hydrogen concentration and curvature change has been reported in previous studies.[4, 6] To estimate the internal stress generated in the Pd layer due to this curvature change, we utilized Stoney's equation, which establishes the relationship between residual stress and curvature variation:[6]

$$\Delta\sigma_{Pd}(H) = \frac{E_x t_x^2}{6t_{Pd}(1-\upsilon_x)}\Delta\kappa(H) \qquad (S5)$$

In this expression, *Δκ(H)* represents the curvature change as a function of hydrogen concentration, *E* is Young's modulus, *t* is the thickness of the layer, and *ν* is Poisson's ratio. The subscripts '*x*' and '*Pd*' refer to the substrate and the palladium film, respectively.

We then performed simulations using COMSOL Multiphysics to validate our analytical model. Initially, a two-dimensional simulation was carried out to reduce computational complexity while

preserving the essential mechanical characteristics of the structure. As described in the main text, Ge was used as a sacrificial layer to enable the release of the cantilever structure, whereas SiO_2 functioned as the anchor region to enhance mechanical robustness and minimize undercutting during the release process. Due to differences in deposition characteristics, a height mismatch developed at the junction between the SiO_2 and Ge films. Subsequent deposition of the cantilever layers over this non-uniform surface led to the formation of a distinct topographical feature at the interface (Figure S1(a)). An elevation-like structure was observed near the junction, resulting from the metal conformally coating the step created by the height difference. To accurately account for this fabrication-related effect, a bump was introduced into the simulated cantilever geometry (Figure S1(b)). The final model represented a Cr/Cu/Cr/Pd microcantilever switch with a ruthenium (Ru) tip and incorporated a bump near the anchor region. Solid mechanics physics was applied, with fixed constraint at the cantilever anchor. The initial stress and strain values for each layer were adopted from earlier calculations. The simulation reproduced the slight upward curvature observed in the fabricated cantilevers showing good agreement with predictions from Equation S4.

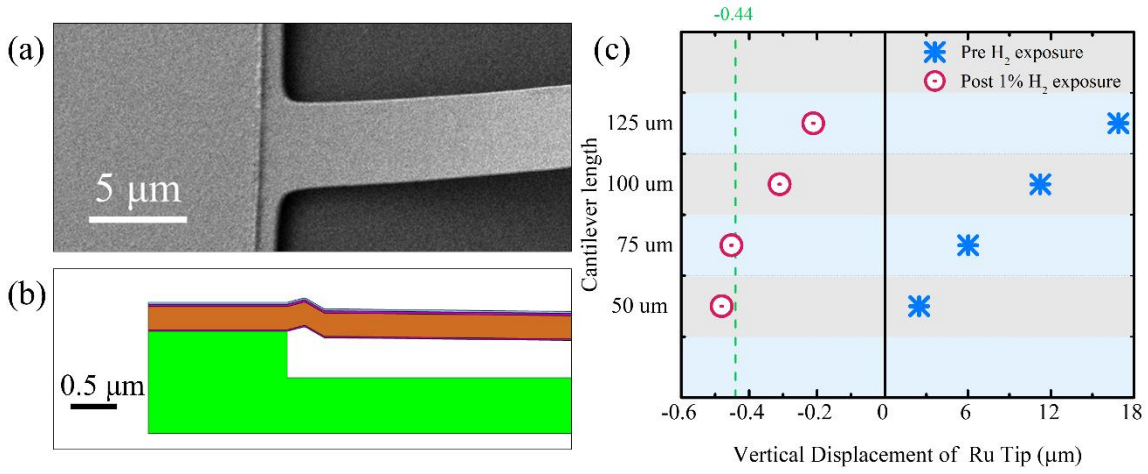

Figure S1: (a) SEM image of the anchor region of a fabricated cantilever. A height mismatch developed at the junction between the SiO_2 and Ge films, leading to the formation of a distinct topographical elevation at the interface during the subsequent deposition of the cantilever layers over the non-uniform surface. (b) Anchor geometry used in the two-dimensional COMSOL simulation of the cantilever. A bump-like structure was introduced to replicate the elevation feature observed in the SEM image. (c) Vertical displacement of the Ru tip under ambient and 1% H_2 in N_2 conditions. Negative displacement values indicate downward bending of the cantilever, with the tip positioned below the anchor. The simulation reveals that only the 50 µm and 75 µm long cantilevers establish contact with the fixed bottom electrode under 1% H_2 exposure.

The deformed geometry from the initial simulation was used as the starting point for a second simulation to simulate the curvature change due to hydrogen absorption. The stress gradient obtained from the first step was also employed. The stress change due to hydrogen absorption was introduced in the Pd layer, as the other layers do not significantly absorb hydrogen and thus exhibit negligible residual stress changes[4]. A stationary study was conducted using solid mechanics physics and the same fixed constraint. Simulation results (Figure S1c) for 1% hydrogen concentration showed that cantilevers of lengths 50 μm and 75 μm bent sufficiently to establish contact with the bottom electrode, enabling current flow. In contrast, the 100 μm and 125 μm cantilevers remained open due to a small curvature change. The vertical separation between the bottom of the Ru tip and the top of the bottom Pt electrodes was 130 nm and 230 nm for the 100 μm and 125 μm long cantilevers, respectively. Thus, contact is only possible for the shorter cantilevers at this hydrogen concentration.

Detailed Fabrication Process:

Our devices are fabricated in the University of Delaware Nanofabrication facility, utilizing standard nanofabrication techniques, including lithography, deposition, and dry etching. The detailed steps of the fabrication process are illustrated in Figure S2, noting that the blocks are not drawn to scale. We used a 650 µm-thick single-side polished <100> silicon wafer with a 300 nm thermal oxide layer as substrate.

The fabrication involves five maskless lithography steps and is described below:

1. The thermal oxide substrate was cleaned using isopropyl alcohol (IPA), acetone, and deionized (DI) water in a hot bath maintained at 80°C, accompanied by ultrasonication (Figure S2(a)). Following the cleaning, a 1-µm-thick layer of silicon dioxide (SiO_2) was deposited onto the substrate at 350 °C using plasma-enhanced chemical vapor deposition (PECVD). Subsequently, a layer of LOR 5A liftoff resist and AZ1512 positive photoresist (PR) was applied via spin coating and subjected to pre-baking on a baking plate. The sacrificial layer is then patterned utilizing pattern 1 through exposure and development processes (Figure S2(b)).

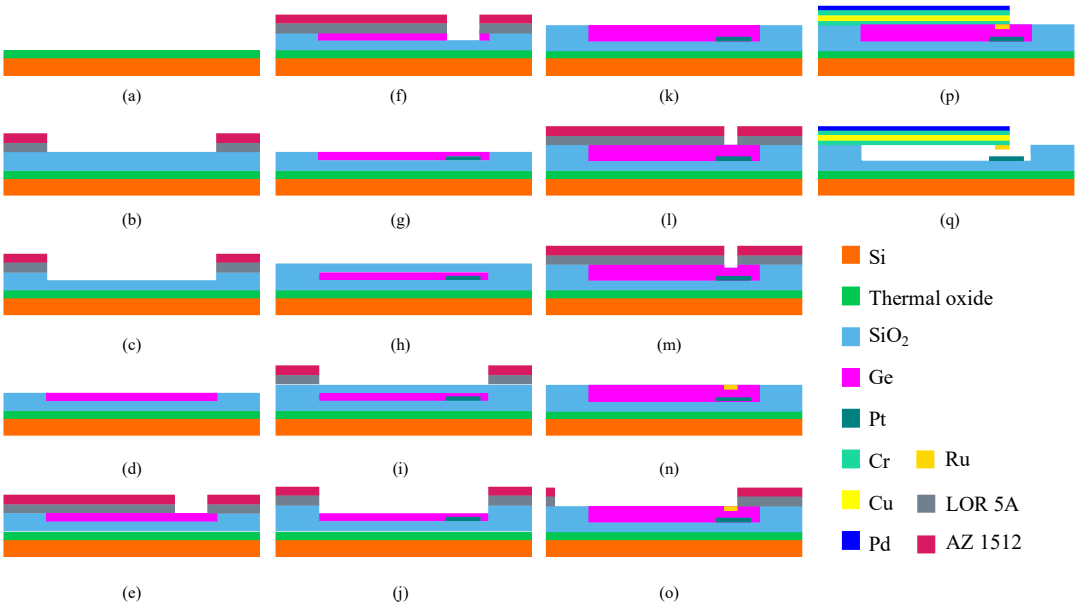

Figure S2: Detailed zero-power bistable hydrogen actuated MEM switch fabrication process

2. Following this, fluorine-based inductively coupled plasma (FICP) etching was employed to etch 200 nm of the patterned SiO_2 layer. Subsequently, a 200 nm-thick Ge layer was deposited using electron beam (e-beam) evaporation using the same pattern (Figures S2(c) and S2(d)). The etching gases utilized during the FICP process include CHF_3 and CF_4, and the recipe had been optimized to achieve a high selectivity ratio of 1.22 for SiO_2 to PR while maintaining a steep sidewall profile.

3. Post-liftoff, the spin coating of LOR 5A liftoff resist, and AZ1512 positive photoresist (PR) was performed, followed by the pre-baking process. The bottom contact layer was subsequently patterned through exposure and development using pattern 2(Figure S2(e)). Further FICP etching is then performed on the patterned Ge layer (Figure S2(f)), culminating in the deposition of 60 nm of platinum (Pt), 4nm of Ni and an additional 140 nm of Germanium. Sulfur hexafluoride (SF_6) gas is utilized to etch the Ge layer, with the recipe optimized for high selectivity of Ge to SiO_2 and PR.

4. Following another liftoff procedure (Figure S2(g)), a 300 nm layer of PECVD SiO_2 was deposited at 350 °C (Figure S2(h)). The application of LOR 5A liftoff resist, and AZ1512 PR was repeated, establishing the same sacrificial layer pattern by utilizing pattern 1 through exposure and development (Figure S2(i)). Afterward, 300 nm of the patterned SiO_2 layer was subjected to FICP etching, after which 300 nm of Ge was deposited using e-beam evaporation (Figure S2(j)).

5. A protruded pattern is then created utilizing the established spin-bake and development workflow employing pattern 3 (Figure S2(l)). This section is subsequently etched by FICP to remove 50 nm of Ge, followed by the deposition of 50 nm of Ru via e-beam evaporation (Figure S2(m)).

6. After another liftoff process (Figure S2(n)), the cantilever structure was subjected to final patterning using identical spin-bake and development techniques employing pattern 4. The sequential deposition process included chromium Cr, Cu, Cr, and Pd using an e-beam evaporation tool (Figure S2(p)). Following the liftoff procedure, FICP is employed to etch the Ge sacrificial layer isotropically, thus effectively releasing the cantilevers (Figure S2(q)). CF_4 is used as the etching gas in a unique bias and pressure configuration to facilitate isotropic etching without compromising the integrity of other device layers.

Multi-cantilever system:

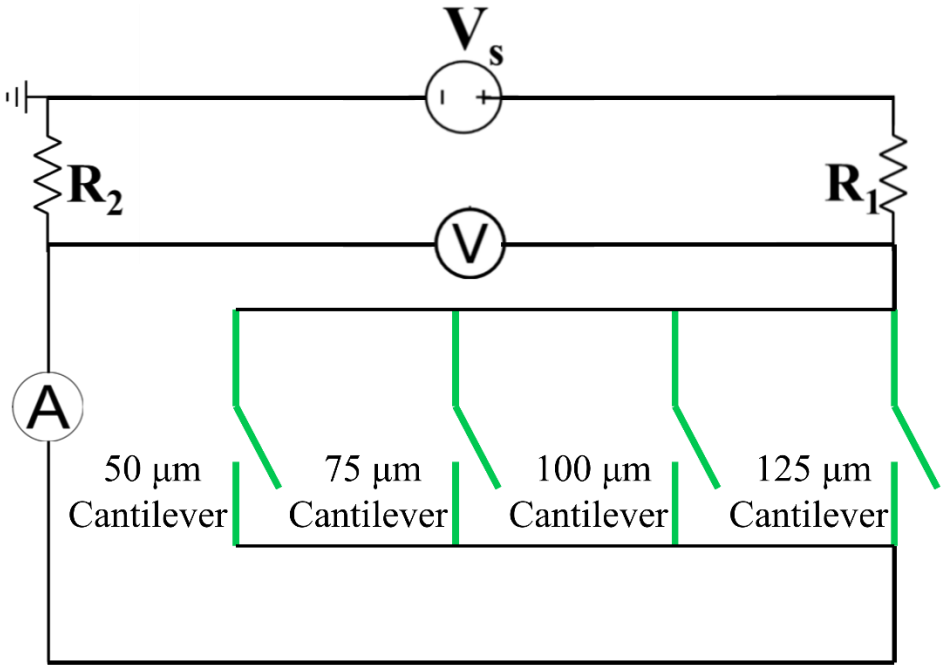

Figure S3: Circuit diagram of a multi-cantilever system. Four independent cantilever switches of lengths 50, 75, 100, and 125 µm were connected in parallel during the measurement steps to quasi-quantify the H_2 concentration level.

References

[1] T. Graham, *Philosophical Transactions of the Royal Society of London* **1997**, *156*, 399.
[2] Y. Chen, Y. Hou, G. Govor, O. Demidenko, Y. Li, *ChemElectroChem* **2024**, *11*, e202400071.
[3] A. Zalineeva, S. Baranton, C. Coutanceau, G. Jerkiewicz, *Langmuir* **2015**, *31*, 1605.
[4] H. Li, Y. Li, K. Wang, L. Lai, X. Xu, B. Sun, Z. Yang, G. Ding, *International Journal of Hydrogen Energy* **2021**, *46*, 1434.
[5] D. R. Baselt, B. Fruhberger, E. Klaassen, S. Cemalovic, C. L. Britton, S. V. Patel, T. E. Mlsna, D. McCorkle, B. Warmack, *Sensors and Actuators B: Chemical* **2003**, *88*, 120.
[6] S. J. McKeown, X. Wang, X. Yu, L. L. Goddard, *Microsystems & Nanoengineering* **2017**, *3*, 16087.